POLITECNICO DI TORINO
Repository ISTITUZIONALE

Quantum-Enhanced Pattern Recognition

Original
Quantum-Enhanced Pattern Recognition / Ortolano, G., Napoli, C., Harney, C., Pirandola, S., Leonetti, G., Boucher, P., Losero, E., Genovese, M., Ruo-Berchera, I.. - In: PHYSICAL REVIEW APPLIED. - ISSN 2331-7019. - 20:2(2023). [10.1103/physrevapplied.20.024072]

Availability:
This version is available at: 11583/2981702 since: 2023-09-06T09:38:29Z

Publisher:
APS

Published
DOI:10.1103/physrevapplied.20.024072

Terms of use:

This article is made available under terms and conditions as specified in the corresponding bibliographic description in the repository

Publisher copyright
APS postprint/Author's Accepted Manuscript e postprint versione editoriale/Version of Record

This article appeared in PHYSICAL REVIEW APPLIED, 2023, 20, 2, and may be found at ttp://dx.doi.org/10.1103/physrevapplied.20.024072. Copyright 2023 American Physical Society

(Article begins on next page)

25 November 2026

Editors' Suggestion

Quantum-Enhanced Pattern Recognition

Giuseppe Ortolano,[1,2,*] Carmine Napoli,[1] Cillian Harney,[3] Stefano Pirandola,[3] Giuseppe Leonetti,[1,2] Pauline Boucher,[1] Elena Losero,[1] Marco Genovese,[1] and Ivano Ruo-Berchera[1]

[1] *Quantum Metrology and Nano Technologies Division, INRiM, Strada delle Cacce 91, Torino 10153, Italy*
[2] *DISAT, Politecnico di Torino, Corso Duca degli Abruzzi 24, Torino 10129, Italy*
[3] *Department of Computer Science, University of York, York YO10 5GH, United Kingdom*

(Received 14 April 2023; revised 11 June 2023; accepted 21 July 2023; published 29 August 2023)

The challenge of pattern recognition is to invoke a strategy that can accurately extract features of a dataset and classify its samples. In realistic scenarios, this dataset may be a physical system from which we want to retrieve information, such as in the readout of optical classical memories. The theoretical and experimental development of quantum reading has demonstrated that the readout of optical memories can be significantly enhanced through the use of quantum resources (namely, entangled input states) over that of the best classical strategies. However, the practicality of this quantum advantage hinges upon the scalability of quantum reading, and up to now its experimental demonstration has been limited to individual cells. In this work, we demonstrate quantum advantage at a fixed resource, namely, at fixed mean probe energy, in the multicell problem of pattern recognition. Through experimental realizations of digits from the Modified National Institute of Standards and Technology (MNIST) handwritten digit dataset, and the application of advanced classical postprocessing, we report the use of entangled probe states and photon counting to achieve quantum advantage in classification error over that achieved with classical resources, confirming that the advantage gained through quantum sensors can be sustained throughout pattern recognition and complex postprocessing. This motivates future developments of quantum-enhanced pattern recognition of bosonic loss within complex domains.

DOI: 10.1103/PhysRevApplied.20.024072

I. INTRODUCTION

Significant progress has been made in recent years in quantum sensing [1–3], a broad spanning field of research which seeks to realize quantum protocols for estimation [4–8] and discrimination [9–12] that achieve better performance than any classical protocol, i.e., gain a quantum advantage. Efforts to design and engineer such protocols have been widely successful, with applications in data readout [13–22], target detection [23–36], cryptography [37,38], fundamental physics research [39–41], and imaging [42–44].

An application of particular interest is that of quantum reading, which encompasses the challenge of classical information retrieval from an optical memory. A memory cell can be considered as a reflective (or transmissive) target with two distinct possible reflectivities (transmittivities) encoding a classical bit. This represents a pair of possible bosonic-lossy channels that act on incident photonic probe states. Accurate readout of a memory cell requires the correct discrimination of output states from the channel (i.e., quantum channel discrimination). Having conceptualized this model, Pirandola [13] proved that one can significantly enhance the accuracy of information retrieval through the use of entangled light sources. This seminal work led to a series of advancements and, most recently, a successful experimental demonstration [20].

The success of quantum reading prompted the development of further schemes in more complex domains, such as the simultaneous readout of many memory cells. This breeds the task of quantum multichannel discrimination [45,46], in which one must optimize multimode probe states and measurements in order to classify a collection of bosonic-lossy channels (or *channel patterns*). This development brings new layers of complication: expanding the space of possible channel patterns to be discriminated, and revealing a more general spectrum of multimodal discrimination protocols. This invites new applications in which quantum reading may serve as a primitive.

The use of quantum sensors within the task of pattern recognition provides such an opportunity, where one is tasked with classifying a set of patterns (or images). The pattern distribution is often nonuniform, and classifications follow highly nonlinear relationships, e.g., the

*g.ortolano@inrim.it

 © 2023 American Physical Society

classification of hand-written digits. Powerful classical postprocessing techniques are well known for this challenge; however, the quality of the readout of datasets is often taken for granted. Given a system that can be modeled as an ensemble of bosonic-lossy multichannels, it has been theoretically shown that quantum reading can substantially enhance classification power over optimal classical strategies at a fixed probing energy [47–51].

In this work, we report the experimental demonstration of quantum-enhanced pattern recognition using signal-idler entangled two-mode squeezed vacuum (TMSV) states and photon-counting (PC) measurements to outperform any classical strategy. Using the Modified National Institute of Standards and Technology (MNIST) handwritten digit dataset [52], image samples are experimentally realized and serve as a testbed for the discrimination protocols. Investigating both multishot and single-shot regimes, we show that the use of entangled probe states can generate quantum advantage in the classification error as a consequence of the gain offered by quantum resources in sensing. By considering multiple supervised-learning approaches to classification, we emphasize that this advantage is an inherent property of quantum sensing that can survive throughout complex postprocessing. Our work paves the way for a suite of near-term applications of quantum-enhanced pattern recognition and imaging.

II. RESULTS

Let us consider a pattern classification problem where spatial patterns are imprinted on a $d \times d$ array of binary cells, each encoding one bit of information in two values of a physical parameter, for example, the transmittances τ_0 and τ_1, where we pose $\tau_0 \leq \tau_1$ [see Fig. 1(a)]. The size of the cells and the dimension of the array d^2 can be native characteristics of the physical support, but also they can be practically determined by resolution properties of the sensing apparatus—for example, the pixel structure of a camera or the resolution of an optical system—so that τ_0 and τ_1 are intended as the values corresponding to each readout pixel. The sensing strategy has to be designed to minimize the average classification error probability of the patterns, P.

The general sensing procedure can be described as in Fig. 1(a). An input state, represented by the density operator ρ, interacts with the object encoding the pattern, and a positive operator-valued measure (POVM) measurement is performed on the output state, followed by classical postprocessing. The state ρ is generally bipartite in order to include ancillary assisted schemes. The two systems are indicated as signal (S) and idler (I), according to quantum-optics terminology. Since we are dealing with bosonic systems, the problem is nontrivial only if we impose some constraints on the resources, the most natural one being to fix the mean number of signal photons, μ, probing the

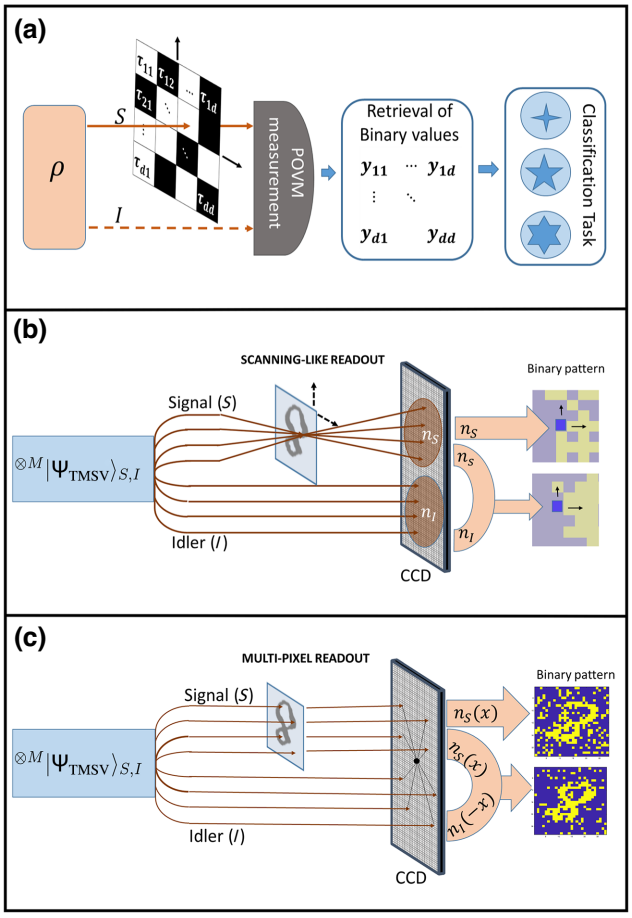


FIG. 1. Scheme of pattern recognition. (a) The general configuration of a pattern recognition problem. An image composed of binary pixels, having one of two possible values of transmittance $\tau_{i,j} = \{\tau_0, \tau_1\}$, is probed by a bipartite state ρ. The signal (S) system interacts with the image. The idler (I) system is directly sent to the measurement apparatus, where a joint measurement is performed with the signal. The result of the measurement is processed classically to classify the patterns. (b) A possible experimental configuration, in which the pattern is "scanned" with sequential single-pixel PC measurements, where n_S and n_I are the signal and idler numbers of photons detected. (c) A different configuration in which the spatial multimode structure of the source is used, so that a parallel readout of all the pixels of the image is done in a single shot. The pairwise quantum correlation of the different modes, represented schematically by the brown arrows hitting symmetric points of the CCD, are used to enhance the classification.

cell. The pixels are assumed to be probed by independent spatial modes, and in this work we restrict our analysis to local measurements, i.e., independent readout is performed for each pixel at the receiver.

Following the local measurement, a binary value is assigned to each pixel with a certain average probability of error p. The binary image is then classified. The classification error P is related to the bit-flip probability p by a,

generally, nonlinear map $\mathcal{M}_C$:

$$P = \mathcal{M}_C(p). \tag{1}$$

The map $\mathcal{M}_C$ depends on the problem at hand, but it is reasonable to assume it monotonic for any effective classification algorithm.

The nonlinearity of the classification algorithms means that they can be surprisingly robust to noise in some ranges, or extremely sensitive to it in other ranges. At the same time, quantum enhancement is independently a function of the bit-flip probability. Thus it is worth investigating this interplay; namely if, for example, there is a region in which there is both a quantum advantage and the classification is sensitive to the noise. Moreover, another layer of complexity is added by the fact that our aim is to relate the classification error to the physical parameters of the system.

Using the monotonicity of $\mathcal{M}_C$, the minimization of P is obtained by minimizing p over all possible input states and POVM measurements. Details on the single-pixel problem are provided in Sec. IV A.

The theoretical lower bound on the error probability achievable by classical states, $p_{\rm cla}^{\rm LB}$, is reported in Eq. (3). It can be saturated, without idler assistance, by a single-mode coherent state $|\alpha\rangle$, and an optimal measurement consisting in the projection on two pseudo-cat states [Eqs. (13) and (14)] as shown in Sec. IV B.

Such a measurement appears to be experimentally unfeasible and no other receiver that saturates $p_{\rm cla}^{\rm LB}$ has been proposed so far. Nevertheless, a photon counting receiver, composed of PC measurement followed by a Bayesian decision, can be proven to perform close to the optimal one for practical purposes [20]. As the PC is a phase-insensitive measurement, it follows that any state with Poisson photon number distribution can reach the PC limit, $p_{\rm cla}^{\rm PC}$, as reported in Eq. (6). For this reason, we use a PC receiver to experimentally perform the pixel readout with both classical and quantum states.

The quantum readout was performed using a collection of M replicas of TMSV states, $\rho_{\rm qua} = |\Psi_{\rm TMSV}\rangle_{S,I}\langle\Psi_{\rm TMSV}|^{\otimes M}$, with

$$|\Psi_{\rm TMSV}\rangle_{S,I} \propto \sum_n \sqrt{P_{\mu_0}(n)}\,|n\rangle_S|n\rangle_I. \tag{2}$$

Here $P_{\mu_0}(n) = \mu_0^n/(\mu_0+1)^{n+1}$ is the thermal distribution with $\mu_0 = \mu/M$ mean photons. In the quantum case, idler assistance is crucial and it is actually convenient to spread the signal energy across a large number of modes, i.e., to work with $M \gg 1$ and $\mu_0 \ll 1$ [20]. The corresponding error probability $p_{\rm qua}^{\rm PC}$, discussed in Sec. IV A, can be evaluated numerically.

Among the various experimental imperfections, the most relevant is photon loss due to nonideal optical component and detector inefficiency. The effect of the losses on classical readout performances is equivalent to a rescaling of the energy, namely, the input mean photon number is substituted by the detected photons, $\mu \to \eta\mu$ in the classical bounds of Eqs. (3) and (6), where η is the overall photon detection probability. However, the quantum strategy is additionally affected by deterioration of the bipartite nonclassical correlation due to losses, which describes the imperfect coupling of correlated modes into the detectors. This effect is discussed in Sec. II C.

A. Experimental realization

The principle of the experimental scheme is presented in Figs. 1(b) and 1(c). The M-product TMSV quantum state $\rho_{\rm qua}$ is produced by traveling-wave spontaneous parametric down-conversion (SPDC) of type II in a nonlinear crystal pumped by a continuous laser. Because of the conservation of the transverse momentum of the pump $\mathbf{q} = 0$, it follows that $\mathbf{q}_S = -\mathbf{q}_I$, i.e., signal and idler photons are emitted along correlated directions (spatial modes), which are mapped into symmetric pixels of a CCD camera. In our experiment, the exposure time of image acquisition is much longer than the coherence time of the process, so many temporal modes, on the order of 10^{11}, contribute to the total number of photons detected in each pixel (a few thousands). Clearly, the conditions $M \gg 1$ and $\mu_0 \ll 1$ which maximize the quantum advantage are fulfilled and the single-pixel photon statistics is practically indistinguishable from the Poisson one. For this reason, the best classical performance with PC detection can be evaluated by considering only the signal beam. Details on the experimental setup are reported in Sec. IV E.

In general, traveling-wave SPDC is spatially broadband. There are many (several thousands) pairwise-correlated spatial modes available for spatially resolved multipixel quantum readout [53,54]. However, a tradeoff should be set between the spatial resolution, in terms of pixels available in one-shot measurement, and the reduction of the pixel error probability due to quantum correlation. This point is discussed later on in the main text, and further details can be found in Sec. IV.

To address this tradeoff, we have realized the experiment in two different configurations, one named "scanninglike readout" [Fig. 1(b)] that favors the best quantum enhancement, and the second one named "multipixel readout" [Fig. 1(c)] that allows spatially resolved pattern acquisitions within a single-shot measurement.

B. Scanninglike Readout

In this first experimental configuration, we mimic a readout in which the physical binary pattern encoded by the transmittance τ_0 and τ_1 is scanned point-by-point, as shown in Fig. 1(b). First, we repeated a large number of independent measurements of two well-characterized transmittances, τ_0 and τ_1, assigning a bit value ($y = 0, 1$)

for each measurement according to the Bayes rule in Eq. (4) based on the number of photon counts n_S and n_I (see Sec. IV A). The photon counts are integrated over two large regions of the CCD array, defining the size of the readout pixel, collecting a large number of signal and idler spatial modes, respectively, obtaining the best possible correlation between n_S and n_I, as discussed in Sec. IV D. This produces two sets of data, $A_0 = \{y_k^{(0)}\}_{k=1,\dots,K}$ and $A_1 = \{y_l^{(1)}\}_{l=1,\dots,L}$, for the nominal transmittances τ_0 and τ_1, respectively, with $L + K \gg d^2$. The procedure is performed for both classical (only using signal beam) and quantum reading.

From those sets we can evaluate the average experimental readout pixel error probabilities, $p_{\rm cla}^{\rm PC}$ and $p_{\rm qua}^{\rm PC}$, shown in Fig. 2(a). One of the transmittances is fixed to $\tau_1 = 1$ while the other one, τ_0, is varied. All other parameters are kept fixed. The experimental points for both the quantum (blue) and classical (red) readouts are compared with the classical lower bound $p_{\rm qua}^{\rm LB}$ (green) defined by Eq. (3). As expected, in general, the error probability increases as the two transmittances become closer and closer. However, through the range of parameters shown, the strategy employing quantum states noticeably outperforms the classical one paired with the suboptimal PC measurement and is also able to surpass the absolute classical lower bound. For the sake of completeness, in Fig. 2(b) we report the same pixel error probabilities in an almost ideal scenario where the detection efficiency is fixed to $\eta = 0.97$ (the efficiency reached in the actual setup is $\eta \approx 0.79$).

Note that the data picked from the sets A_0 and A_1 can be virtually rearranged to reproduce the outcomes of a sequential spatial scanning of any given $d \times d$ binary pattern. However, for an accurate evaluation of the pattern recognition task, the used approach is highly preferable with respect to the real scanning of spatial samples. In fact, the last one would require the physical realization and scanning of a large number of spatial samples, which is hardly feasible and actually not necessary.

To evaluate the pattern recognition performance, we used the MNIST handwritten digit dataset, containing 60 000 training samples of handwritten numerical digits and 10 000 test samples. We assemble the entire set of test patterns by picking experimental data from the set A_0 and A_1. Figure 3 shows some examples of digits contained in the dataset, and a comparison of the effect of the noise in either a classical or a quantum binary readout.

For the classification of the noisy digits, we used a k-nearest-neighbor (k-NN) classifier [55]. A k-NN classifier computes the distance between the pattern tested and all the patterns in its training set. In the case of binary patterns, the most natural metric is the Hamming distance. The k closest patterns of the training set to the tested pattern are selected, and the class of the test pattern is assigned as the more common among the k closest. The experimental

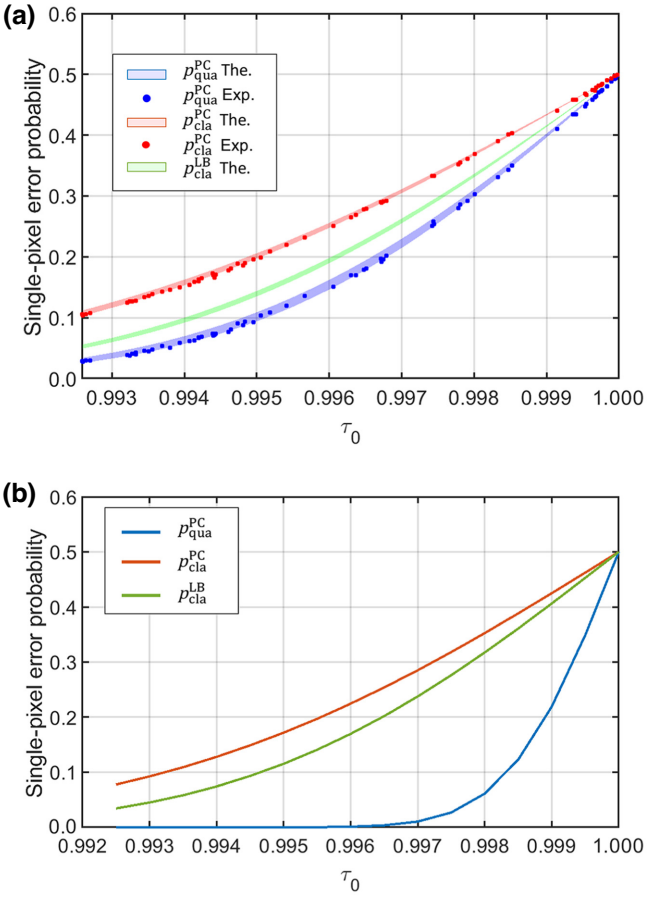


FIG. 2. Single-pixel readout error probabilities. (a) The error probability in the readout of a bit encoded in the transmittance value (either τ_0 or τ_1) of a single pixel. The lower transmittance, τ_0, is varied while the other one is fixed to $\tau_1 = 1$. The estimated mean number of photons per pixel is $\mu = (1.45 \pm 0.05) \times 10^5$, the efficiencies are $\eta_S = 0.79 \pm 0.01$ and $\eta_I = 0.791 \pm 0.004$, and the electronic noise is $\nu \approx 6 \times 10^3$. The probability of error for the quantum strategy is reported in blue, the classical strategy with photon counting in red, and the best classical strategy in green. The confidence interval of the theoretical curves is obtained by considering one standard deviation on the reported parameters. (b) The theoretical prediction on the error probabilities in the almost ideal case of $\eta_S = \eta_I = 0.97$, while all the other parameters are the same as in panel (a).

classification error is reported in Fig. 4(a) as a function of the transmittance τ_0; while in Fig. 4(b) we report the classification performance in the almost ideal ($\eta = 0.97$) detection scenario. Note that the performance of the k-NN classifier is highly nonlinear with respect to the single-pixel error probability. For the values of τ_0 corresponding to a classical error probability $p_{\rm cla}^{\rm PC} < 0.3$ in Fig. 2(a), the classification is very robust to noise. In this range, the classification error is almost negligible for all the strategies and the quantum advantage is also rather small. However, for higher transmittance τ_0, the algorithm becomes very sensitive to the readout noise level and here the advantage of

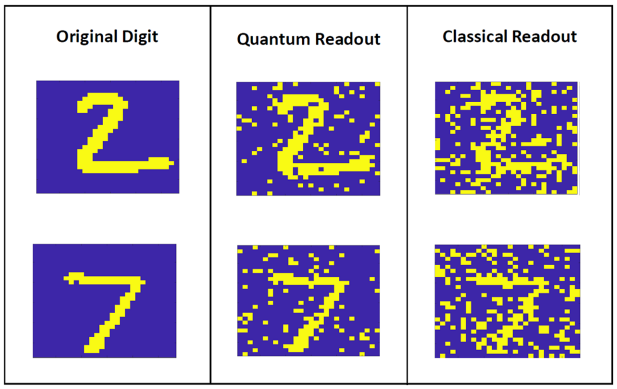


FIG. 3. Readout of handwritten digits with different strategies. Two examples of binary patterns of dimension 28×28 with quantum and classical PC readout noise.

quantum strategy is amplified. In fact, the experimental quantum advantage in the pattern recognition task, represented in Fig. 4(c), reaches up to 4 dB, which is much larger than the corresponding pixel error improvement.

At this point, the following question arises. Is the amplification of the quantum advantage in sensing we have observed for the k-NN classifier a property of this specific classifier, or a more general behavior characterizing the pattern classification task? To partially address this question, we repeat our analysis with another classification strategy that uses a refined machine-learning approach.

Convolutional neural networks (CNNs) are a category of feed-forward neural networks that are omnipresent in the field of image processing, and are a particularly powerful tool for pattern recognition [56,57]. They contain hidden layers that convolve input data from one layer to the next, in which the convolutions are performed according to parameterized filters (or kernels). The goal of learning is to optimize these filters in such a way that complex features can be reliably extracted and classified. This form of network architecture helps to minimize the number of network parameters and also helps the CNN to interpret features in a translationally invariant way, i.e., qualities inferred in one area of an image can be reused elsewhere in the image.

In this work, we apply CNN classifiers to the task of noisy pattern recognition on the MNIST dataset as before with the k-NN classifier, considering experimental input data from quantum-enhanced and classical sensors. We trained a collection of classifiers on a noisy training set in which each pixel in an image undergoes a bit flip with single-pixel error rate of p_{train}, i.e., the single-pixel training error. Meanwhile, the network parameter optimization was carried out by backpropagation using a cross-entropy loss cost function. More precisely, we prepared a set of 16 CNNs, whose p_{train} was distributed across the interval $[0, 0.5]$. The single-pixel training error is a particularly influential parameter as fine-tuning p_{train} helps classifiers to become more robust to noise and to learn how to reduce its impact on classification [58]. The classifiers could then be evaluated on the experimental test sets (constructed from A_0 and A_1) in order to quantify the performance of quantum-enhanced versus classical pattern recognition.

The results of the CNN strategy are presented in Fig. 5. Figure 5(a) compares the performance of the classical and quantum-enhanced classifiers. We have a collection of CNN classifiers which have been trained using different single-pixel training errors, denoted by $\{\mathsf{C}[p_{\text{train}}]\}_{p_{\text{train}}\in[0,0.5]}$. It follows that some classifiers can garner better performance than others. Ideally, we would claim the classification error associated with the best classifier from our set, i.e., $\mathsf{C}[p_{\text{train}}^{\text{max}}]$. But this approach remains unrealistic, since it is not possible to predict *a priori* what the best p_{train} would be. Instead, we may use the single-pixel error rates associated with the chosen discrimination protocol to motivate our choice of training error rate at a given transmissivity τ_0, constructing the classifiers $\mathsf{C}[p_{\text{train}}^{\text{theory}}]$ (for more details, see Sec. IV D). Figure 5(b) plots these corresponding values against the single-pixel transmissivity.

Finally, Fig. 5(c) reports the quantum advantage in the pattern recognition task (in decibels) showing a similar behavior to that observed in Fig. 4(c). This confirms that the quantum advantage gathered through the single-pixel readout can be sustained throughout complex postprocessing techniques, such as CNN training and evaluation.

C. Parallel Multipixel Readout

While the scanninglike readout of the previous subsection represents a meaningful proof of principle necessary for a clean and faithful comparison with the theory, here we consider a more realistic scenario of a multipixel parallel readout, as depicted in Fig. 1(c), where the pattern is acquired in a single shot.

The samples, containing digits from 0 to 9, were realized on an antireflection-coated glass slide combining laser lithography, sputtering deposition of titanium in high vacuum, and a liftoff technique. The transmittance of the deposition is estimated as $\tau_0 = 0.987 \pm 0.003$. The parallel readout is doable since the state ρ_{qua} produced by SPDC is spatially multimode. Pairwise-correlated modes are detected by symmetric pairs of pixels in the CCD chip as represented in Fig. 1(c), so that a thousand pixel pairs are in principle nonclassically correlated at the same time. However, to efficiently collect the correlated modes, the size of the pixel l_D should be larger than the transverse cross-correlation length l_c of the source. The consequence is a tradeoff between the obtainable spatial resolution and the quantum advantage in the single-pixel readout. We set the pixel size of our camera to fulfill the condition $l_D > l_c$

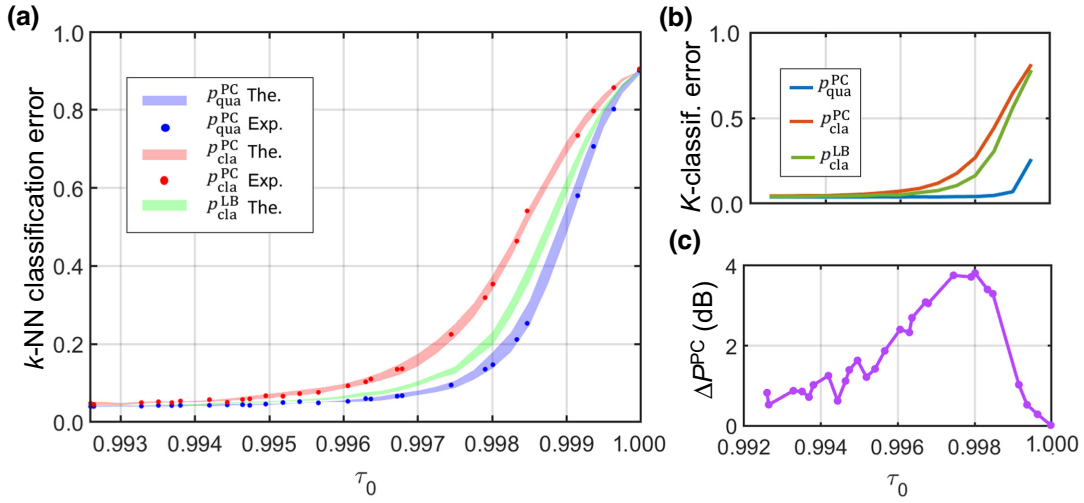


FIG. 4. Classification error with the k-NN algorithm. (a) The average classification error P in the recognition of handwritten digits encoded in binary transmittance values (τ_0 and τ_1). The lower transmittance, τ_0, is varied, while $\tau_1 = 1$. Experimental points are reported for the quantum (blue) and classical (red) PC readouts along with the theoretical predictions. The green band reports a simulation of the performance obtained with a pixel readout at the absolute classical limit. (b) The classification error for almost ideal efficiency, $\eta = 0.97$. (c) The experimental quantum advantage, in decibels ($\Delta P^{\mathrm{PC}} := -10\log_{10}(P^{\mathrm{PC}}_{\mathrm{qua}}/P^{\mathrm{PC}}_{\mathrm{cla}})$).

and at the same time to have a 28×28 image of the digits (more details are presented in Sec. IV D).

Figure 6(a) shows the experimental pixel error probabilities for both classical and quantum PC readout as a function of the effective transverse resolution at the sample plane. The effective resolution is changed by applying a moving-average filter to the acquired images, as described in Sec. IV D, which has practically the same effect as increasing the pixel size. On the one hand, increasing the pixel size has the direct consequence of raising the number of signal photons per pixel, which explains the decrease of the classical error probability, according to Eq. (6). On the other hand, as clearly shown in Fig. 6(a), the quantum error probability decreases faster than the classical analogue, because the detectable quantum correlation increases while losing spatial resolution. Here, the comparison of the experimental results with the theoretical bounds is not straightforward and we will avoid it. In fact,

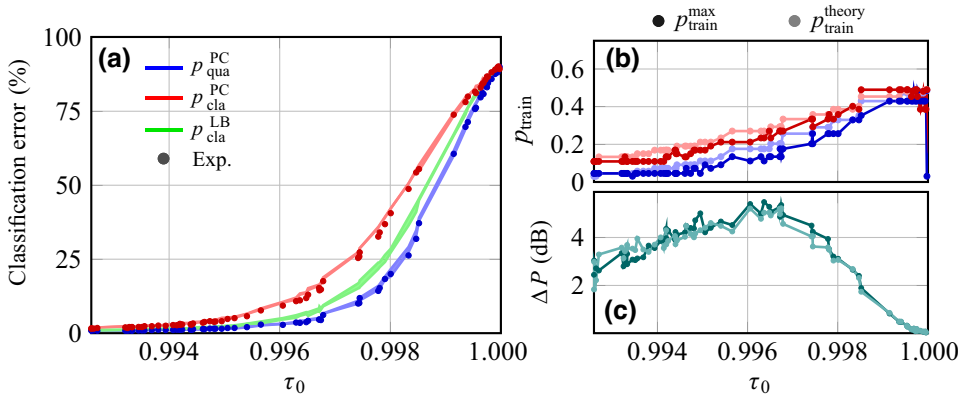


FIG. 5. Quantum-enhanced pattern recognition via the CNNs. (a) The classification error of CNNs on the MNIST using sensors with quantum resources (blue) or classical resources (red). We trained 16 CNNs on noisy training sets of 60 000 images with single-pixel errors in the interval $p_{\mathrm{train}} \in [0, 0.5]$. We used these CNNs to classify a test set of 10 000 images simulated at different single-pixel transmissivities, τ_0. The solid lines portray the simulated classification error region associated with a CNN using a single-pixel training error predicted by the corresponding theoretical single-pixel error bounds $p^{\mathrm{theory}}_{\mathrm{train}}$ at τ_0. Experimental data points are plotted for both quantum and classical photon-counting protocols. (b) Plots of both the theory-predicted value and the best-choice value for p_{train}. (c) Plots of the experimental quantum advantage ΔP in decibels obtained with using TMSV states over classical coherent states (and photon counting). The darker points plot the advantage between CNNs that use the best-choice $p^{\mathrm{max}}_{\mathrm{train}}$ while the lighter points plot the advantage gained using theory-predicted $p^{\mathrm{theory}}_{\mathrm{train}}$.

when binary patterns are read out with finite resolution, for a detection pixel that falls across the edge between τ_0 and τ_1 the binary model is no longer valid. Such border effects are not negligible as the resolution decreases and become comparable with the spatial features of the pattern. These features are very difficult to account for in a theoretical model.

We evaluated the pattern recognition performance once again on the MNIST handwritten digit dataset using a k-NN algorithm for the classification. While the test dataset is composed of 10 000 patterns, producing and acquiring 10 000 samples is not feasible and is an unnecessary task. In fact, the error in the classification can be broken down into two contributions. The first contribution is intrinsic to the classification algorithm, and the second comes from the noise in the readout. In our case, with a pixel error larger than about 0.3, the classification error is dominated by the noise in sensing. For reference, the classification error without noise is on the order of 4%, while in the noisy region it is clearly much larger. So, we assume that the classification error can be well studied by printing a small subset of patterns from the original MNIST, namely 10, and performing on each of them 1000 different acquisitions with independent noise realizations, forming a total dataset of 10 000 images.

The resulting classification error is reported in Fig. 6(b) as a function of the spatial resolution. The results are reported up to a resolution of 39 μm, which is equivalent to an effective reduction of the resolution of a factor of 3 with respect to the original dataset. Confirming the main results of the previous section, in a sensing scenario dominated by quantum noise, a relatively small quantum enhancement in the single-pixel probability (namely, from 0.35 to 0.32) can be amplified to around 20% in the classification.

III. DISCUSSION AND CONCLUSION

In this work, we have experimentally demonstrated the advantage of quantum-enhanced sensing in the task of pattern recognition. As a testbed, we have considered the problem of classification of handwritten digits. A quantum readout strategy based on TMSV states and PC measurement leads to a relevant advantage in the classification errors with respect to any classical sensing.

We have realized the experiment in two different configurations. In the first one, called "scanninglike readout," we have chosen to concentrate on the magnitude of the quantum advantage rather than the acquisition time, since scanning of the sample is required. In this case, we were able to clearly beat the optimal classical bound. In the second configuration, instead, we have considered single-shot multipixel readout of the pattern. In this case, we have shown a large advantage with respect to the classical bound that uses photon counting.

Moreover, the presence of quantum advantage turns out to be independent of the complexity of the classification algorithm. Having deployed both k-NN classifiers (a simple and robust strategy) and CNN classifiers (a machine-learning enhanced strategy) on the same experimental data, similar results are obtained: quantum advantage in the sensing is maintained and often amplified in the pattern recognition task.

The results presented here pave the way for studies of applications in biological spatial pattern recognition and prompt further experimental investigation of quantum-enhanced pattern recognition in the spectral and temporal domains.

IV. MATERIALS AND METHODS

A. Single-pixel readout

The single-pixel problem has been extensively analyzed in Refs. [13,15,16,20,22]. In the following, we will compare three different local readout strategies.

In the first scenario, we consider classical input states $\rho_{\rm cla}$, i.e., a mixture of coherent states, paired with a theoretical optimal POVM Λ. The optimal probability of error in discriminating the outcome states $\rho_{\rm cla}(\tau_0)$ and $\rho_{\rm cla}(\tau_1)$ can be derived by the Helstrom bound [4], $(1 - D(\rho_0, \rho_1))/2$, where ρ_0 and ρ_1 are two generic states, and $D(\rho_0, \rho_1)$ is the trace distance. Using the convexity of $D(\rho_0, \rho_1)$, Ref. [13] demonstrated the following bound to the classical error probability:

$$p_{\rm cla}^{\rm LB} = \frac{1 - \sqrt{1 - \exp(-\mu_0(\sqrt{\tau_0} - \sqrt{\tau_1})^2)}}{2} \tag{3}$$

where μ_0 is the mean number of signal photons. As discussed in Ref. [13], ancillary modes cannot enhance the performance of the readout with classical states. In fact, the bound in Eq. (3) can be obtained by using a single-mode coherent state transmitter, $\rho_{\rm cla} = |\alpha\rangle\langle\alpha|$, with $|\alpha|^2 = \mu_0$, as shown in Sec. IV B.

However, the optimal measurement, which we discuss in Sec. IV B, is purely theoretical, and no feasible receiver has been proposed yet to reach the classical lower bound in Eq. (3). Thus, we consider a second, more practical, scenario where the receiver is based on photon-counting measurements, which can be proven to perform close to the optimal one for practical purposes [20]. The conditional photon number distribution at the receiver is $p(\mathbf{n}|\tau_i) = \langle\mathbf{n}|\rho(\tau_i)|\mathbf{n}\rangle$, where $\mathbf{n} = (n_S, n_I)$ is the number of measured photons in the signal and idler (the ancilla) systems. The optimal choice to recover the value of the bit j is to choose it according to the Bayes rule:

$$j = arg\, max_i p(\tau_i|\mathbf{n}). \tag{4}$$

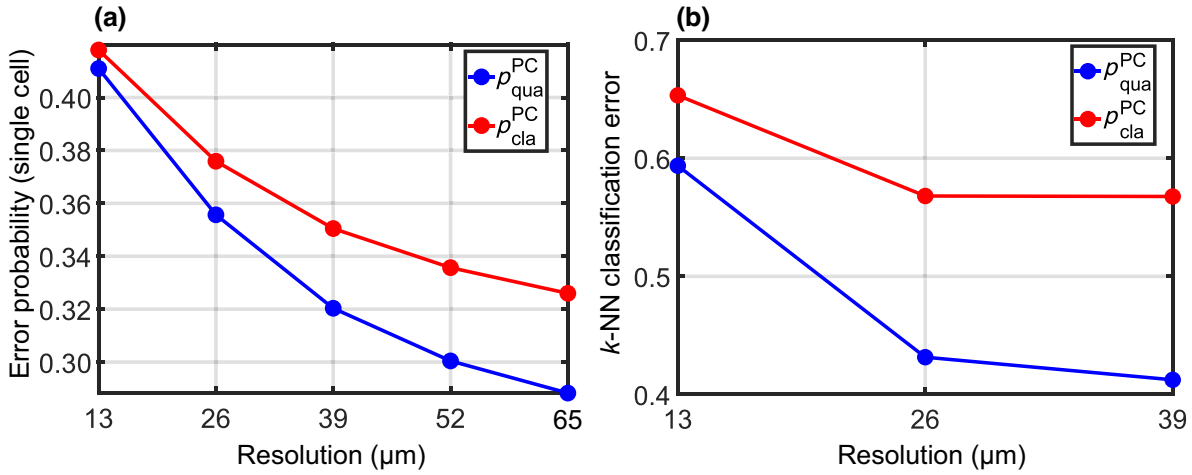


FIG. 6. Multipixel readout performance as a function of the spatial resolution. (a) The single-pixel error probability decreases with the resolution at the object plane. The mean number of photons per pixel per frame, at full resolution (13 μm), is $\mu = 1380 \pm 20$, while the total channel efficiencies of signal and idler branches are $\eta_S = 0.795 \pm 0.01$ and $\eta_I = 0.815 \pm 0.01$. The pattern transmittance level is fixed to $\tau_0 = 0.987 \pm 0.003$. (b) The error in the pattern classification with a k-NN algorithm.

This condition is equivalent to the maximum-likelihood decision $j = arg\, max_i p(\mathbf{n}|\tau_i)$ in the balanced prior probability case. The error probability with photon-counting receiver is given by

$$p^{\mathrm{PC}} = \frac{1}{2}\sum_{\mathbf{n}} \min_i p(\mathbf{n}|\tau_i), \tag{5}$$

i.e., proportional to the overlap of the measurement outcome distributions, $p(\mathbf{n}|\tau_0)$ and $p(\mathbf{n}|\tau_1)$.

As for the optimal classical case, the conditional distribution overlap cannot be reduced by using the ancillary mode, and the overlap is minimized for input signal states having the photon statistics of a coherent state, i.e., a Poisson distribution $\mathcal{P}_{\mu_0}(n)$, where μ_0 is the mean number of photons [20]. The statistics of the photons returning from a cell of transmittance τ_i still follows the Poisson distribution, in particular, $\mathcal{P}_{\mu_0\tau_i}(n_s)$. Substituting this into the conditional probabilities of Eq. (5), the best performance achievable with classical states and PC measurements is [20]

$$p^{\mathrm{PC}}_{\mathrm{cla}} = \frac{1}{2} - \frac{\Gamma(\lfloor n^{\mathrm{th}}+1\rfloor, \mu_0\tau_0) - \Gamma(\lfloor n^{\mathrm{th}}+1\rfloor, \mu_0\tau_1)}{2\lfloor n^{\mathrm{th}}\rfloor!} \tag{6}$$

where $\Gamma(x,y)$ is the incomplete gamma function, $\lfloor x\rfloor$ is the floor of x, and $n^{\mathrm{th}} := \mu_0(\tau_1-\tau_0)/\log(\tau_1/\tau_0)$ is the intersection point of the two Poisson distributions $\mathcal{P}_{\mu_0\tau_0}$ and $\mathcal{P}_{\mu_0\tau_1}$.

The third strategy we consider here uses a collection of M replicas of two-mode squeezed vacuum states in the input, $\rho_{\mathrm{qua}} = |\Psi_{\mathrm{TMSV}}\rangle_{S,I}\langle\Psi_{\mathrm{TMSV}}|^{\otimes M}$, with $|\Psi_{\mathrm{TMSV}}\rangle_{I,S} \propto \sum_n \sqrt{P_{\mu_0}(n)}\,|n\rangle_S|n\rangle_I$ and $P_{\mu_0}(n) = \mu_0^n/(\mu_0+1)^{n+1}$ being a thermal distribution with μ_0 mean photons. The joint probability of signal and idler photons of a TMSV state after the interaction with the cell of transmittance τ_i is $p_{\mu_0}(n_S, n_I|\tau_u) = P_{\mu_0}(n_I)\mathcal{B}(n_S|n_I,\tau_i)$, where $\mathcal{B}$ stands for the binomial distribution. For the multimode state ρ_{qua}, the joint distribution is simply obtained by substituting the single-mode thermal statistics $P_{\mu_0}(n_I)$ with a multithermal one, $P_{\mu_0,M}(n_I)$, obtained by the convolution of M thermal modes. The conditional joint probability evaluated in this way can be substituted in Eq. (5) to obtain the error of the quantum strategy, $p^{\mathrm{PC}}_{\mathrm{qua}}$. This quantity can be evaluated numerically. It turns out that, for a fixed total number of photons transmitted to the cell $\mu_0 M$, the most effective way to exploit quantum correlation is to span the photons in a large number of modes so that $\mu_0 \ll 1$ and $M \gg 1$. Moreover, the local multithermal distribution approaches the Poisson one. This is the regime that we consider in the simulation, and the one that is realized in the experiment.

B. Optimal local receiver for classical states

The single-pixel readout probability of error that can be reached with classical states, having a fixed number of signal photons μ, is lower-bounded by the limit in Eq. (3). As previously mentioned, this limit can be saturated by using a single-mode coherent state without idlers. This can be seen using the fact that a pure loss channel, with transmissivity τ, maps a coherent state $|\alpha\rangle$ into another, amplitude-damped, coherent state $|\sqrt{\tau}\alpha\rangle$. Once the input state ρ_{in} is fixed, the discrimination of two channels having different transmissivities is reduced to a binary quantum-state discrimination between the two possible outputs, ρ_0 and ρ_1, for which the lowest error probability is given by

the Helstrom formula,

$$p^H = \frac{1}{2}(1 - \|\pi_0\rho_0 - \pi_1\rho_1\|), \tag{7}$$

where $\|\cdot\|$ is the trace distance and π_0 and π_1 are the prior probabilities.

For coherent input, the potential outputs of the channel are pure and their trace distance can be expressed in terms of the overlap $\zeta = \langle\sqrt{\tau_0}\alpha|\sqrt{\tau_1}\alpha\rangle = \exp(-\frac{1}{2}\mu(\sqrt{\tau_0} - \sqrt{\tau_1})^2)$ as

$$\begin{aligned}&\| \pi_0|\sqrt{\tau_0}\alpha\rangle\langle\sqrt{\tau_0}\alpha| - \pi_1|\sqrt{\tau_1}\alpha\rangle\langle\sqrt{\tau_1}\alpha| \| \\ &\quad = \sqrt{1 - 4\pi_0\pi_1|\zeta|^2}.\end{aligned}$$

Substituting this into Eq. (7) and setting equal priors $\pi_0 = \pi_1 = 1/2$ we get

$$p_{\text{coh}} = \frac{1 - \sqrt{1 - |\zeta|^2}}{2}, \tag{8}$$

which coincides with $p^{\text{LB}}_{\text{cla}}$, proving that a single-mode coherent state saturates the classical bound (originally proven for an arbitrary P-representation [13]).

The optimal probability of error is achieved by projecting into the eigenstates of the Hermitian operator:

$$\Lambda = \frac{1}{2}(|\sqrt{\tau_0}\alpha\rangle\langle\sqrt{\tau_0}\alpha| - |\sqrt{\tau_1}\alpha\rangle\langle\sqrt{\tau_1}\alpha|). \tag{9}$$

We can find an orthogonal basis to represent Λ by performing the Gram-Schmidt orthogonalization on the pair of vectors $(|\sqrt{\tau_0}\alpha\rangle, |\sqrt{\tau_1}\alpha\rangle)$ spanning its support. So we define the basis:

$$|0\rangle = |\sqrt{\tau_0}\alpha\rangle, \quad |1\rangle = \frac{|\sqrt{\tau_1}\alpha\rangle - \zeta|\sqrt{\tau_0}\alpha\rangle}{\sqrt{1 - |\zeta|^2}}. \tag{10}$$

The eigenvectors of Λ can be computed with simple algebra to be, in terms of this basis,

$$|+\rangle = \frac{1}{\sqrt{2}}\sqrt{1 - \sqrt{1 - \zeta^2}}\,|0\rangle - \frac{1}{\sqrt{2}}\sqrt{1 + \sqrt{1 - \zeta^2}}\,|1\rangle, \tag{11}$$

$$|-\rangle = \frac{1}{\sqrt{2}}\sqrt{1 + \sqrt{1 - \zeta^2}}\,|0\rangle + \frac{1}{\sqrt{2}}\sqrt{1 - \sqrt{1 - \zeta^2}}\,|1\rangle. \tag{12}$$

Then substituting the definitions in Eq. (10) leads to

$$|+\rangle = \sqrt{\frac{1 - \sqrt{1 - \zeta^2}}{2(1 - \zeta^2)}}\,|\sqrt{\tau_1}\alpha\rangle - \sqrt{\frac{1 + \sqrt{1 - \zeta^2}}{2(1 - \zeta^2)}}\,|\sqrt{\tau_0}\alpha\rangle, \tag{13}$$

$$|-\rangle = \sqrt{\frac{1 + \sqrt{1 - \zeta^2}}{2(1 - \zeta^2)}}\,|\sqrt{\tau_1}\alpha\rangle - \sqrt{\frac{1 - \sqrt{1 - \zeta^2}}{2(1 - \zeta^2)}}\,|\sqrt{\tau_0}\alpha\rangle. \tag{14}$$

The bit can then be recovered by measuring over the projectors $\Pi_0 = |+\rangle\langle+|$ and $\Pi_1 = |-\rangle\langle-|$. Once the measurement is performed, the value τ_0 is selected if the outcome is $+$, and τ_1 is selected otherwise. This measurement paired with a coherent state input would in theory saturate the classical bound in Eq. (3). However, as pointed out in the main text, from a practical point of view, an implementation of this kind of measurement would be very complicated, if feasible at all, with current technology.

C. The *k*-NN classification

Let $\boldsymbol{i}_0 = \{b^{(0)}_{ij}\}$ and $\boldsymbol{i}_1 = \{b^{(1)}_{ij}\}$, with $b_{ij} = 0, 1$, be two binary images of dimension $d \times d$. The Hamming distance, d_H, between $\boldsymbol{i}_0$ and $\boldsymbol{i}_1$ is defined as

$$d_H(\boldsymbol{i}_0, \boldsymbol{i}_1) = \sum_{i=1}^{d}\sum_{j=1}^{d} |b^{(0)}_{ij} - b^{(1)}_{ij}|. \tag{15}$$

The k-NN is a supervised classification method that uses the known label of images in a training set $\mathcal{T}$ to assign a class to images in a test set $\mathcal{V}$. Given an image $\boldsymbol{i}_v$ in $\mathcal{V}$, the set of its k closest images in terms of the Hamming distance, $\mathcal{K} = \{\boldsymbol{i}^{(1)}_{\mathcal{T}}, \ldots, \boldsymbol{i}^{(k)}_{\mathcal{T}}\} \subset \mathcal{T}$, is selected from $\mathcal{T}$. The image $\boldsymbol{i}_v$ is assigned to the class c_v that is the most common among the images in $\mathcal{K}$. The most intuitive case is given by the 1-NN classifier, which assigns to the image $\boldsymbol{i}_v$ the same class of its closest image in the training set $\mathcal{T}$.

D. Neural-network classification

Consider a dataset of images $\mathcal{I} := \{\boldsymbol{i}_j\,; c_j\}_j$ in which each image $\boldsymbol{i}_j$ possesses a classification (or label) c_j. For the task of classification, a neural network [59,60] is a universal approximating function $f_{\boldsymbol{\theta}}$ (where $\boldsymbol{\theta}$ denotes the parameter set of the neural network) which takes an image as input and provides an approximation of its classification as an output, $f_{\boldsymbol{\theta}}(\boldsymbol{i}_j) = c'_j$. Training a neural network as a classifier equates to optimizing its parameters $\boldsymbol{\theta}$ such that $f_{\boldsymbol{\theta}}(\boldsymbol{i}_j) \approx c_j$ becomes a reliable classifier over the entire dataset. That is, the goal of training is to maximize the accuracy of the classifier over the training set in such a way that it can generalize to new, unforeseen samples. In a neural network, the parameter set $\boldsymbol{\theta}$ describes correlations between layers of neurons, capable to encoding highly complex relationships between input and output.

When building neural-network classifiers for which there already exist experimental data (as in the case of MNIST), supervised learning is a very effective strategy. This involves utilizing a set of images whose classifications are already exactly known, and training the neural network on these data. In this way, the classifier can be optimized reliably and can extract meaningful features from the dataset in order to learn correlations between input patterns and their classification. The classification

error of the classifier is measured against an evaluation (or test) set, i.e., a set of images that the network has never seen during training and therefore must extrapolate. Given a K-element evaluation set of images and labels $\mathcal{V} = \{\boldsymbol{i}_k; c_k\}_{k=1}^{K}$ and a classifier $f_{\boldsymbol{\theta}}$, then the classification error is approximated as

$$P_{f_{\boldsymbol{\theta}}} = \frac{1}{K}\sum_{k=1}^{K}\delta[f_{\boldsymbol{\theta}}(\boldsymbol{i}_k), c_k], \tag{16}$$

where $\delta[f_{\boldsymbol{\theta}}(\boldsymbol{i}_k), c_k]$ is a Kronecker delta function that returns unity if and only if the classifications are the same, otherwise it will return zero.

In this work, we exploit CNNs as classifiers upon our experimental dataset. Using the Julia Flux package [61, 62], we construct CNNs with three convolutional layers and a dense layer, optimizing a cross-entropy loss function during training. This produces classifiers of sufficient accuracy to utilize in this study. We use the MNIST handwritten digit dataset, composed of a training set $\mathcal{T}$ with 6×10^4 images and an experimental evaluation set $\mathcal{V}$. The experimental dataset is clearly unchangeable and is inherently noisy. But the initially noiseless training set can be manipulated to modify and enhance our classifiers. As discussed in the main text, it is useful to train a CNN on noisy data if it is expected to classify noisy data. To do this, we simulate noisy training sets $\mathcal{T}_{p_{\text{train}}}$ in which each pixel in every image is independently bit-flipped according to the probability p_{train}. We then trained a collection of different classifiers using different values of $p_{\text{train}} \in [0, 0.5]$ and evaluated them on the experimental data.

It is difficult to know what the best-case p_{train} is with respect to the transmissivity of the sampled pixels. As depicted in Fig. 5, we can identify a best-choice classifier from our collection as that which minimizes its classification error with respect to the evaluation set. However, it is not practicable to select a best-choice classifier *a posteriori* (this would defeat the purpose of discrimination). Instead, we present the best-case performance for benchmarking purposes and more practically motivate our chosen p_{train} by mapping the single-pixel transmissivity to a single-pixel error probability associated with the discrimination protocol being used.

E. Experimental setup and noise reduction

Acquisitions for both the experimental configurations reported in Figs. 1(b) and 1(c) are performed using the setup sketched in Fig. 7. It exploits SPDC to generate multimode pairwise-correlated collections of TMSV states, by pumping a type II β-barium borate (BBO) nonlinear crystal with a 100-mW continuous laser at wavelength $\lambda_p = 405$ nm. The SPDC photons are selected around the degenerate wavelength $\lambda = 2\lambda_p = 810$ nm by an interference filter (IF) at (800 ± 20) nm. The correlations in momentum

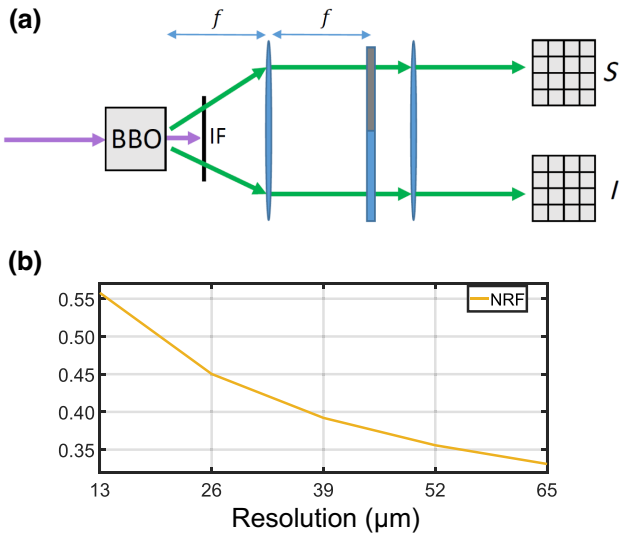


FIG. 7. (a) Schematic of the experimental setup described in Sec. IV E. (b) Noise reduction factor as a function of the effective spatial resolution.

at the source are converted in spatial correlations at the "object" plane, by use of a lens having focal length $f = 1$ cm, in an f–f configuration, performing a Fourier transform on the incoming field. The test patterns to be classified are physically realized as depositions, according to the procedure of Sec. IV F. The patterns are placed in the signal beam at the object plane, while a blank glass slide is placed on the idler beam to match the two optical paths. The object plane is then imaged to the charge-coupled device (CCD) camera using a second lens, with magnification of about 8 times. The camera (Princeton Instruments Pixis 400BR Excelon) has a nominal quantum efficiency >95%, electronic noise of $4e^-$ per pixel per frame and the physical pixel size is 13 μm. The total channel efficiencies η_S and η_I are estimated to be close to 80% according to the procedure outlined in Refs. [63,64].

In the scanninglike configuration, we introduce in the signal beam a variable absorber that is fine-tuned in the range $1 - \tau_0 = 10^{-2}$ to 10^{-3}. Signal and idler photons n_S and n_I are obtained by integrating over two corresponding wide spatial areas composed of a large number of physical pixels, becoming equivalent to two bucket detectors. This leads to the most efficient collection of the correlated photons [21] and thus achievement of a higher quantum advantage, as we will explain in the following.

In contrast, in the parallel multipixel readout, we exploit the spatial resolution of the detector to have a one-shot (without scanning) image of size 28×28 of a test digit in the signal arm, which is the original dimension of the binary images of the MNIST dataset. For that, we perform an 8×8 hardware binning of the physical pixels, to obtain an effective readout pixel of $l_D = 104$ μm, corresponding to a resolution of $l_R = 13$ μm at the object plane (not to

be confused with the original physical pixel size of the detector mentioned earlier).

However, a tradeoff exists between spatial resolution and quantum noise reduction achieved by exploiting the signal-idler correlations. In fact, correlated photons from the multimode SPDC arrive at the detector within a certain transverse spatial uncertainty, which comes from the finite size of the pump beam. For this reason, the signal-idler intensity cross-correlation is well approximated by a Gaussian function with finite coherence length l_c at the detector plane (in our case this is $l_c \sim 40$ μm). To efficiently detect the correlated modes, the pixel size, or more generally the detector resolution area, must be larger than this coherence length, $l_D \geq l_c$ [65].

In Sec. II C we analyze the pattern recognition performance as a function of the resolution. For a fair comparison in the classification, it is more suitable to have final binary images always with the same number of pixels. Thus, instead of changing the resolution by performing a simple pixel binning, we preferred to change it by applying an averaging filter of appropriate size. The averaging filter substitutes for each pixel count, the average of the counts in a neighborhood of size $d \times d$. This is repeated for each original pixel of the 28×28 matrix, so that the final size of the image in terms of pixels is unvaried, although the effective spatial resolution is reduced.

In Fig. 6(a), the parameter d ranges between 1 and 5, which correspond to an effective resolution l_R between 13 and 65 μm. The improvement of the quantum correlations as a function of the image resolution can be witnessed by the noise reduction factor (NRF), defined as $F_{\mathrm{NR}} = \langle \Delta^2(n_S - n_I)\rangle / \langle n_S + n_I\rangle$ [66–70]. The NRF is an indicator of nonclassical correlations, since it can show values in the range $0 < F_{\mathrm{NR}} < 1$ only for nonclassical fields, while it is $F_{\mathrm{NR}} \geq 1$ for classical light. In Fig. 7(b) we report the measured NRF as a function of the effective resolution at the object plane.

F. Handwritten digit deposition

The computer-aided design of the 10 digits (from 0 to 9) was realized by normalizing the dimension of each binary image (28×28 pixel^2) of each digit in squares of maximum dimension of 400×400 μm^2 spaced by 1000 μm. A laser lithography process was performed with Heidelberg Instruments uPG101 system equipped with a UV laser source at 375 nm. The deposition of titanium was carried out by sputtering in high vacuum at low rate (0.08 nm/s). Thicknesses from 2 to 4 nm were deposited to obtain a transmittance value suitable for the experiment. Final patterning was obtained by removing excess titanium through a liftoff technique.

All data needed to evaluate the conclusions are reported in the paper. Further data, for reproducibility of the results, are available [70].

ACKNOWLEDGMENTS

Part of this work (sample fabrication) has been carried out at QR Laboratories, INRiM, a micro- and nanofabrication laboratory. I.R.-B. thanks the INRiM researcher Matteo Fretto for supervising the sample realization.

This work has been founded by the European Union's Horizon 2020 Research and Innovation Action under the Grant Agreement No. 862644 (Quantum readout techniques and technologies, QUARTET) and under the Grant Agreement No. 101113901 (Qu-Test).

G.O. and I.R.-B. devised the present realization of quantum-enhanced pattern recognition, with advice from S.P.; E.L., P.B., C.N., and G.O. performed the experimental acquisitions; G.O. did the data analysis on the experimental data and computed the optimal local measurement to saturate the classical lower bound; G.O. and C.H. performed the classification analysis for k-NN and CNN, respectively; the samples were prepared by G.L.; M.G., head of the INRiM quantum optics sector, and I.R.-B. supervised the project; G.O., I.R.-B., S.P., and C.H. wrote the paper with contributions from all authors.

The authors declare no competing interests.

[1] C. L. Degen, F. Reinhard, and P. Cappellaro, Quantum sensing, Rev. Mod. Phys. **89**, 035002 (2017).

[2] S. Pirandola, B. R. Bardhan, T. Gehring, C. Weedbrook, and S. Lloyd, Advances in photonic quantum sensing, Nat. Photon **12**, 724 (2018).

[3] G. Petrini, E. Moreva, E. Bernardi, P. Traina, G. Tomagra, V. Carabelli, I. P. Degiovanni, and M. Genovese, Is a quantum biosensing revolution approaching? Perspectives in NV-assisted current and thermal biosensing in living cells, Adv. Quantum Technol. **3**, 2000066 (2020).

[4] C. Helstrom, *Quantum Detection and Estimation Theory* (Academic Press, New York, 1976).

[5] S. L. Braunstein and C. M. Caves, Statistical Distance and the Geometry of Quantum States, Phys. Rev. Lett. **72**, 3439 (1994).

[6] S. L. Braunstein, C. M. Caves, and G. Milburn, Generalized uncertainty relations: Theory, examples, and Lorentz invariance, Ann. Phys. **247**, 135 (1996).

[7] V. Giovannetti, S. Lloyd, and L. Maccone, Quantum-enhanced measurements: Beating the standard quantum limit, Science **306**, 1330 (2004).

[8] V. Giovannetti, S. Lloyd, and L. Maccone, Advances in quantum metrology, Nat. Photon **5**, 222 (2011).

[9] C. W. Helstrom, Quantum detection and estimation theory, J. Stat. Phys. **1**, 231 (1969).

[10] A. Chefles and S. M. Barnett, Quantum state separation, unambiguous discrimination and exact cloning, J. Phys. A: Math. Gen. **31**, 10097 (1998).

[11] A. Chefles, Quantum state discrimination, Contemp. Phys. **41**, 401 (2000).

[12] J. A. Bergou, U. Herzog, and M. Hillery, in *Quantum State Estimation* (Springer Berlin Heidelberg, 2004), p. 417.

[13] S. Pirandola, Quantum Reading of a Classical Digital Memory, Phys. Rev. Lett. **106**, 090504 (2011).

[14] S. Pirandola, C. Lupo, V. Giovannetti, S. Mancini, and S. L. Braunstein, Quantum reading capacity, New J. Phys. **13**, 113012 (2011).

[15] R. Nair, Discriminating quantum-optical beam-splitter channels with number-diagonal signal states: Applications to quantum reading and target detection, Phys. Rev. A **84**, 032312 (2011).

[16] C. Invernizzi, M. G. A. Paris, and S. Pirandola, Optimal detection of losses by thermal probes, Phys. Rev. A **84**, 022334 (2011).

[17] M. Dall'Arno, A. Bisio, and G. M. D'Ariano, Ideal quantum reading of optical memories, Int. J. Quantum Inf. **10**, 1241010 (2012).

[18] G. Spedalieri, C. Lupo, S. Mancini, S. L. Braunstein, and S. Pirandola, Quantum reading under a local energy constraint, Phys. Rev. A **86**, 012315 (2012).

[19] J. P. Tej, A. R. U. Devi, and A. K. Rajagopal, Quantum reading of digital memory with non-Gaussian entangled light, Phys. Rev. A **87**, 052308 (2013).

[20] G. Ortolano, E. Losero, S. Pirandola, M. Genovese, and I. Ruo-Berchera, Experimental quantum reading with photon counting, Sci. Adv. **7**, eabc7796 (2021).

[21] G. Ortolano, P. Boucher, I. P. Degiovanni, E. Losero, M. Genovese, and I. Ruo-Berchera, Quantum conformance test, Sci. Adv. **7**, eabm3093 (2021).

[22] G. Ortolano and I. Ruo-Berchera, Quantum readout of imperfect classical data, Sensors **22**, 2266 (2022).

[23] M. F. Sacchi, Entanglement can enhance the distinguishability of entanglement-breaking channels, Phys. Rev. A **72**, 014305 (2005).

[24] S. Lloyd, Enhanced sensitivity of photodetection via quantum illumination, Science **321**, 1463 (2008).

[25] S.-H. Tan, B. I. Erkmen, V. Giovannetti, S. Guha, S. Lloyd, L. Maccone, S. Pirandola, and J. H. Shapiro, Quantum Illumination with Gaussian States, Phys. Rev. Lett. **101**, 253601 (2008).

[26] E. D. Lopaeva, I. Ruo Berchera, I. P. Degiovanni, S. Olivares, G. Brida, and M. Genovese, Experimental Realization of Quantum Illumination, Phys. Rev. Lett. **110**, 153603 (2013).

[27] Z. Zhang, M. Tengner, T. Zhong, F. N. C. Wong, and J. H. Shapiro, Entanglement's Benefit Survives an Entanglement-Breaking Channel, Phys. Rev. Lett. **111**, 010501 (2013).

[28] Z. Zhang, S. Mouradian, F. N. C. Wong, and J. H. Shapiro, Entanglement-Enhanced Sensing in a Lossy and Noisy Environment, Phys. Rev. Lett. **114**, 110506 (2015).

[29] S. Barzanjeh, S. Guha, C. Weedbrook, D. Vitali, J. H. Shapiro, and S. Pirandola, Microwave Quantum Illumination, Phys. Rev. Lett. **114**, 080503 (2015).

[30] M. Sanz, U. Las Heras, J. J. García-Ripoll, E. Solano, and R. Di Candia, Quantum Estimation Methods for Quantum Illumination, Phys. Rev. Lett. **118**, 070803 (2017).

[31] Q. Zhuang, Z. Zhang, and J. H. Shapiro, Entanglement-enhanced Neyman–Pearson target detection using quantum illumination, J. Opt. Soc. Am. B **34**, 1567 (2017).

[32] Q. Zhuang, Z. Zhang, and J. H. Shapiro, Quantum illumination for enhanced detection of Rayleigh-fading targets, Phys. Rev. A **96**, 020302(R) (2017).

[33] S. Barzanjeh, S. Pirandola, D. Vitali, and J. M. Fink, Microwave quantum illumination using a digital receiver, Sci. Adv. **6**, eabb0451 (2020).

[34] M. Casariego, Y. Omar, and M. Sanz, Bi-frequency illumination: A quantum-enhanced protocol, Adv. Quantum Technol. **5**, 2100051 (2022).

[35] Q. Zhuang and J. H. Shapiro, Ultimate Accuracy Limit of Quantum Pulse-Compression Ranging, Phys. Rev. Lett. **128**, 010501 (2022).

[36] T. Gonzalez-Raya and M. Sanz, Coplanar antenna design for microwave entangled signals propagating in open air, Quantum **6**, 783 (2022).

[37] G. Spedalieri, Cryptographic aspects of quantum reading, Entropy **17**, 2218 (2015).

[38] J. L. Pereira and S. Pirandola, Bounds on amplitude-damping-channel discrimination, Phys. Rev. A **103**, 022610 (2021).

[39] A. J. Brady, C. Gao, R. Harnik, Z. Liu, Z. Zhang, and Q. Zhuang, Entangled Sensor-Networks for Dark-Matter Searches, PRX Quantum **3**, 030333 (2022).

[40] M. M. Marchese, A. Belenchia, S. Pirandola, and M. Paternostro, An optomechanical platform for quantum hypothesis testing for collapse models, New J. Phys. **23**, 043022 (2021).

[41] I. Ruo Berchera, I. P. Degiovanni, S. Olivares, and M. Genovese, Quantum Light in Coupled Interferometers for Quantum Gravity Tests, Phys. Rev. Lett. **110**, 213601 (2013).

[42] M. Genovese, Real applications of quantum imaging, J. Opt. **18**, 073002 (2016).

[43] E. Losero, I. Ruo-Berchera, A. Meda, A. Avella, and M. Genovese, Unbiased estimation of an optical loss at the ultimate quantum limit with twin-beams, Sci. Rep. **8**, 7431 (2018).

[44] G. Spedalieri, L. Piersimoni, O. Laurino, S. L. Braunstein, and S. Pirandola, Detecting and tracking bacteria with quantum light, Phys. Rev. Res. **2**, 043260 (2020).

[45] Q. Zhuang and S. Pirandola, Entanglement-enhanced testing of multiple quantum hypotheses, Commun. Phys. **3**, 103 (2020).

[46] Q. Zhuang and S. Pirandola, Ultimate Limits for Multiple Quantum Channel Discrimination, Phys. Rev. Lett. **125**, 080505 (2020).

[47] L. Banchi, Q. Zhuang, and S. Pirandola, Quantum-Enhanced Barcode Decoding and Pattern Recognition, Phys. Rev. Appl. **14**, 064026 (2020).

[48] J. L. Pereira, Q. Zhuang, and S. Pirandola, Optimal environment localization, Phys. Rev. Res. **2**, 043189 (2020).

[49] C. Harney, L. Banchi, and S. Pirandola, Ultimate limits of thermal pattern recognition, Phys. Rev. A **103**, 052406 (2021).

[50] C. Harney and S. Pirandola, Analytical bounds for dynamic multichannel discrimination, Phys. Rev. A **104**, 032402 (2021).

[51] C. Harney and S. Pirandola, Idler-free multi-channel discrimination via multipartite probe states, Npj Quantum Inf. **7**, 153 (2021).

[52] Y. Lecun, L. Bottou, Y. Bengio, and P. Haffner, Gradient-based learning applied to document recognition, Proc. IEEE **86**, 2278 (1998).
[53] G. Brida, M. Genovese, and I. Ruo Berchera, Experimental realization of sub-shot-noise quantum imaging, Nat. Photon **4**, 227 (2010).
[54] N. Samantaray, I. Ruo-Berchera, A. Meda, and M. Genovese, Realization of the first sub-shot-noise wide field microscope, Light: Sci. Appl. **6**, e17005 EP (2017).
[55] T. Cover and P. Hart, Nearest neighbor pattern classification, IEEE Trans. Inf. Theory **13**, 21 (1967).
[56] K. O'Shea and R. Nash, An introduction to convolutional neural networks, arXiv:1511.08458 (2015).
[57] J. Gu, Z. Wang, J. Kuen, L. Ma, A. Shahroudy, B. Shuai, T. Liu, X. Wang, G. Wang, J. Cai, and T. Chen, Recent advances in convolutional neural networks, Pattern Recognit. **77**, 354 (2018).
[58] T. S. Nazaré, G. B. P. da Costa, W. A. Contato, and M. Ponti, in *Progress in Pattern Recognition, Image Analysis, Computer Vision, and Applications*, edited by M. Mendoza and S. Velastín (Springer International Publishing, Cham, 2018), p. 416.
[59] M. A. Nielsen, *Neural Networks and Deep Learning* (Determination Press, 2015), http://neuralnetworksanddeeplearning.com/.
[60] K. P. Murphy, *Machine Learning: A Probabilistic Perspective* (MIT Press, Cambridge, MA, 2012).
[61] M. Innes, E. Saba, K. Fischer, D. Gandhi, M. C. Rudilosso, N. M. Joy, T. Karmali, A. Pal, and V. Shah, Fashionable modelling with Flux, CoRR **abs/1811.01457** (2018), arXiv:1811.01457.
[62] M. Innes, Flux: Elegant machine learning with Julia, J. Open Source Software **3**, 602 (2018).
[63] G. Brida, I. Degiovanni, M. Genovese, M. L. Rastello, and I. Ruo-Berchera, Detection of multimode spatial correlation in PDC and application to the absolute calibration of a CCD camera, Opt. Express **18**, 20572 (2010).
[64] A. Avella, I. Ruo-Berchera, I. P. Degiovanni, G. Brida, and M. Genovese, Absolute calibration of an EMCCD camera by quantum correlation, linking photon counting to the analog regime, Opt. Lett. **41**, 1841 (2016).
[65] A. Meda, E. Losero, N. Samantaray, F. Scafirimuto, S. Pradyumna, A. Avella, I. Ruo-Berchera, and M. Genovese, Photon-number correlation for quantum enhanced imaging and sensing, J. Opt. **19**, 094002 (2017).
[66] O. Jedrkiewicz, Y.-K. Jiang, E. Brambilla, A. Gatti, M. Bache, L. A. Lugiato, and P. Di Trapani, Detection of Sub-Shot-Noise Spatial Correlation in High-Gain Parametric Down Conversion, Phys. Rev. Lett. **93**, 243601 (2004).
[67] M. Bondani, A. Allevi, G. Zambra, M. G. A. Paris, and A. Andreoni, Sub-shot-noise photon-number correlation in a mesoscopic twin beam of light, Phys. Rev. A **76**, 013833 (2007).
[68] J.-L. Blanchet, F. Devaux, L. Furfaro, and E. Lantz, Measurement of Sub-Shot-Noise Correlations of Spatial Fluctuations in the Photon-Counting Regime, Phys. Rev. Lett. **101**, 233604 (2008).
[69] I. N. Agafonov, M. V. Chekhova, and G. Leuchs, Two-color bright squeezed vacuum, Phys. Rev. A **82**, 011801 (2010).
[70] J. Peřina, M. Hamar, V. Michálek, and O. c. v. Haderka, Photon-number distributions of twin beams generated in spontaneous parametric down-conversion and measured by an intensified CCD camera, Phys. Rev. A **85**, 023816 (2012).
[71] https://doi.org/10.5281/zenodo.8212062.